# 3-D imaging of the Balmuccia peridotite body (Ivrea–Verbano zone, NW-Italy) using controlled source seismic data

Trond Ryberg [1], Christian Haberland,[1] Britta Wawerzinek [1], Manfred Stiller,[1] Klaus Bauer,[1] Alberto Zanetti,[2] Luca Ziberna,[2,3] György Hetényi [4], Othmar Müntener,[4] Michael M. Weber[1] and Charlotte M. Krawczyk[1,5]

[1] *GFZ German Research Centre for Geosciences, Telegrafenberg,* 14473 *Potsdam, Germany.* E-mail: *trond@gfz-potsdam.de*
[2] *Istituto di Geoscienze e Georisorse, Consiglio Nazionale delle Ricerche, Via Ferrata* 1, 27100 *Pavia, Italy*
[3] *Department of Mathematics and Geosciences, University of Trieste, Via Weiss* 2, 34128 *Trieste Trieste, Italy*
[4] *Institute of Earth Sciences, University of Lausanne, Géopolis,* 1015 *Lausanne, Switzerland*
[5] *Institute for Applied Geosciences, TU Berlin, Ernst-Reuter-Platz* 1, 10587 *Berlin, Germany*

## SUMMARY

We provide new results from a controlled-source seismic experiment on the deepest part of the Val Sesia crust–mantle section of the Ivrea–Verbano zone (IVZ) in the Italian Alps. The IVZ is a tilted, almost complete section through the continental crust and exposes gabbros and peridotites in the structurally deepest level, coinciding with high-resolution gravity anomalies imaging the Ivrea geophysical body. The seismic experiment SEIZE (SEismic imaging of the Ivrea ZonE) was conducted along two crossing profiles: an NNE-SSW profile of ∼11 km length and an E-W profile of ∼16 km length. 432 vibration points were recorded with 110 receivers resulting in 24 392 traveltime picks. Inversion methods using Markov chain Monte Carlo techniques have been used to derive an isotropic 3-D $P$-wave velocity model based on first break traveltimes (refracted phases) from controlled source seismic data. Resulting seismic $P$-wave velocities ($V_p$) range from 4.5 to 7.5 km s$^{-1}$, with an expected general trend of increasing velocities with depth. A sharp velocity change from low $V_p$ in the West to high $V_p$ in the East marks the Insubric Zone (ISZ), the Europe–Adria plate boundary. The most prominent feature of the 3-D tomography model is a high-velocity body ($V_p$ increases from 6 to 7.5 km s$^{-1}$) that broadens downwards. Its pointy shape peaks the surface East of Balmuccia at a location coincident with the exposed Balmuccia peridotite. Considering rock physics, high-resolution gravity and other geophysical data, we interpret this high-velocity body as dominantly composed of peridotite. The dimension of this seismically imaged peridotite material is far bigger than interpreted from geological cross-sections and requires a revision of previous models. The interpretation of ultramafic bodies in the IVZ as fragments of mantle peridotites interfingered in the crust during pre-Permian accretion is not supported by the new data. Instead, we revive a model that the contact between the Balmuccia peridotite and the Permian mafic magmas might represent a fossil continental crust–mantle transition zone.

**Key words:** Europe; Controlled source seismology; Seismic tomography; Continental tectonics: compressional; Crustal structure.

## 1 INTRODUCTION

The nature and evolution of the lower continental crust and its transition to the mantle, including migration and emplacement of magmas, are still not unequivocally resolved (Mereu *et al.* 1989; Rudnick & Fountain 1995; Artemieva & Shulgin 2019, and references therein). The Ivrea–Verbano Zone (IVZ) in the Italian Alps (Fig. 1) is one of the most complete and most studied, time-integrated archetypes of continental crust–upper-mantle sections on Earth. It provides one of the best natural laboratories to significantly advance our understanding of the crust–mantle transition zone. It is accessible and, in addition to geological indicators of exposed mantle rocks, geophysical anomalies point to a shallow subsurface position of Earth upper mantle (Berckhemer 1968; Rivalenti *et al.*
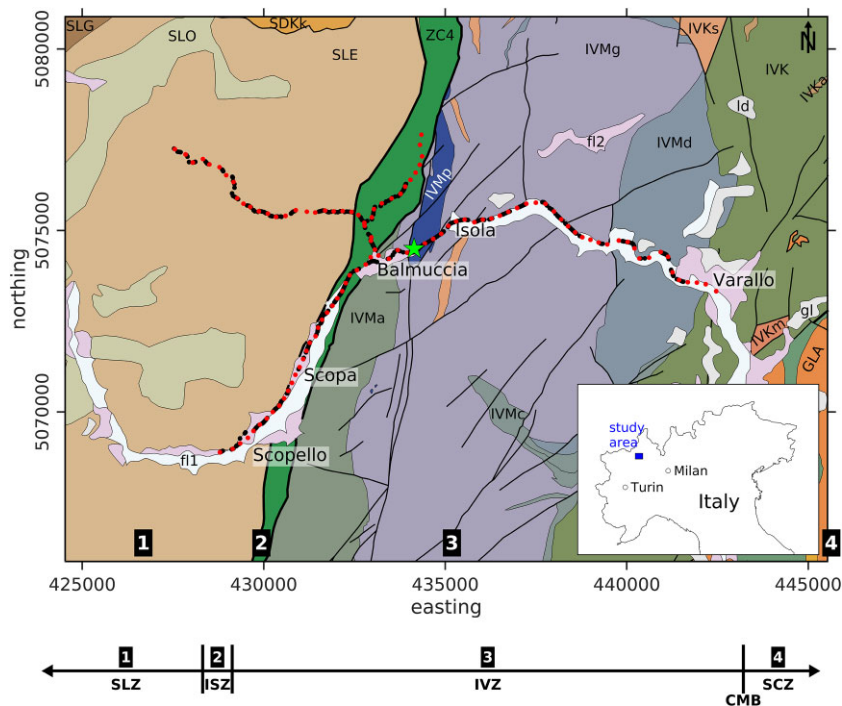
**Figure 1.** Top: geological map of the Balmuccia area, Val Sesia, Southern IVZ (after Piana *et al.* 2017a,b, and references therein, Quick *et al.* 2003) overlain with sources and receivers for orientation (red/black dots) and the planned drilling location DT-2 (green star). Most geological units in the area dip at high angle from horizontal (>60°, Horstmann 1981; Quick *et al.* 2003). Black numbered squares mark the different geological zones (bottom).The abbreviations/colours of the lithological units correspond to Piana *et al.* (2017a,b):

*Quaternary*: fl1 ■—alluvial and debris flow deposits; fl2 ■—terraced alluvial and debris flow deposits; gl ■—glacial deposits and ld ■—landslides accumulations.

*Sesia Lanza Zone (SLZ)*: SDKk ■—paragneiss; SLE ■—mica schist and paragneiss; SLG ■—gneiss; SLO ■—orthogneiss.

*Canavese zone* (segment of the ISZ): ZC4 ■—mylonitic rocks and cataclasite.

*Ivrea Verbano Zone (IVZ)—Mafic complex*: IVMa ■—peridotite, pyroxenite, gabbro, gabbroic rocks; IVMc ■—granite, granodiorite and granofels; IVMd ■—diorite; IVMg ■—gabbro and granulite and ■ IVMp –peridotite.

*Ivrea Verbano Zone (IVZ)—Kinzigite formation*: IVKa ■—amphibolite; IVK ■—gneiss and mica schist; IVKm ■—marble and IVKs ■—granodiorite and granulite.

*SCZ—Permian magmatic complex*: GLA ■—granite.The CMB line divides the lower and upper crustal rocks. Modified from Geoportale Arpa Piemonte—GeoPiemonte Map 2021 (https://webgis.arpa.piemonte.it/agportal/apps/webappviewer/index.html?id = 6ea1e38603d6469298333c2efbc76c72).

1981; Lanza 1982; Kissling 1984; Schmid *et al.* 1996, 2017; Zingg 1983; Diehl *et al.* 2009; Decarlis *et al.* 2017; Scarponi *et al.* 2020, 2021).

Geochemical and petrological analyses of outcrop samples and modelling illustrate that the IVZ is a precious archive of trans-crustal continental magmatism documenting lower crustal processes of magma emplacement, crystallization and crustal assimilation (e.g. Rivalenti *et al.* 1981; Voshage *et al.* 1990; Sinigoi *et al.* 1994; Sinigoi *et al.* 2011). These processes have been linked to near-surface magmatism, including evidence for protracted super-eruptions during the Permian (Quick *et al.* 2009).

Exposed crust–mantle transition zones also enable a thorough geophysical and petrological investigation of spatial and temporal relationships between rock units of the lower crust which cannot be obtained by xenolith investigations alone. Indeed, lower crustal magmatic underplating linked to the formation of upper crustal magma reservoirs can only be studied in a few cross-sections worldwide, most of which are incomplete and to our current knowledge none of them displays a complete Moho transition zone (Salisbury & Fountain 1990). They nevertheless provide important clues about the nature of the lowermost continental crust and the Moho itself as a physico-chemical filter. For instance, they are useful in understanding the variation of chemical and physical properties with depth in the crust, including heat production (Galson 1983; Ashwal *et al.* 1987; Fountain *et al.* 1987), seismic velocities (Fountain 1976; Kern & Schenk 1985; Chroston & Simmons 1989; Lu *et al.* 2018), density (Kissling 1984; Scarponi *et al.* 2020) and magnetic susceptibility (Wasilewski & Fountain 1982; Williams *et al.* 1985; Shive & Fountain 1988). These data, coupled with the geometry of rock units, form the basis of geophysical models of the crust and the hypotheses concerning the chemical and physical identity of Earth's crust. For example, seismic models based on exposed cross-sections (Fountain 1976; Hale & Thompson 1982; Christensen & Mooney 1995; Rutter *et al.* 1999; Behn & Kelemen 2006; Liu *et al.* 2021) and experimental petrology (Müntener & Ulmer 2006) indicate that large variations of seismic velocity associated with compositionally variable lithologic layers could be responsible for the pronounced seismic reflectivity in the lower crust (e.g. Bois *et al.* 1989).

The IVZ is unique in that several geophysical observables indicate near subsurface presence of high density and high seismic velocity rocks (Berckhemer 1968; Lanza 1982; Diehl *et al.* 2009; Scarponi *et al.* 2021). This has raised broad interest the further analysing the rocks, including in the near subsurface, which has converged to a scientific drilling project (Pistone *et al.* 2017), in which one of the targets is the crust–mantle transition. With project SEIZE (SEismic imaging of the Ivrea ZonE) we aim, therefore, at delineating at

high resolution the depth, extent and shape of the anomalous rocks at the Balmuccia peridotite site in Val Sesia, Italy (Fig. 1) and its relation to geophysical anomalies hitherto resolved at much lower resolution and depth uncertainty. This target was chosen as the depth extent of the Balmuccia peridotite has been extrapolated based on surface geological observations and has generally been considered as an isolated lensoidal body of ca. 4.4 km length, ca. 0.6 km width and ca. 1 km depth, mixed with other lithologies of the lower crust (Quick *et al.* 1995, 2003).

A preliminary seismic survey in the area has not imaged the bottom of the body (Liu *et al.* 2021). Seismological data (Diehl *et al.* 2009) reveal a Moho uplift beneath the IVZ, but there is no evidence of a connection of the Ivrea geophysical body (IGB) to the surface due to the lack of resolution. Petrological modelling suggests that crustal rocks might be expected at significant depth (Pistone *et al.* 2020), however gravity and passive seismic data indicate dense and high-velocity rocks as close as ∼1 km beneath the surface (Scarponi *et al.* 2020, 2021). Determining the shape of the Balmuccia peridotite and whether it continues to several kilometres depth, together with the downward continuation of the adjacent, steeply dipping Insubric Zone (ISZ), is crucial in testing the hypothesis of a discontinuous peridotite body versus a peridotite body connected to the deeper IGB. The overall objective of SEIZE and the planned drilling project is to elucidate the nature of the continental lower crust, its transition to the mantle, and to provide a geophysical characterization of rock properties.

## 2 GEOLOGICAL SETTING

The IVZ is a tectonic sliver in the Southern Alps made of high-grade metamorphic and plutonic rocks mostly of Permian and pre-Permian age (Fig. 1). To the West, it is bordered by the ISZ, which separates the IVZ from the basement of the South-Austroalpine domain (Schmid *et al.* 1987; Nicolas *et al.* 1990). To the East, it is juxtaposed by the Cossato–Mergozzo–Brissago (CMB) and the Pogallo Lines (Boriani & Sacchi 1973; Zingg 1983; Handy 1987; Snoke *et al.* 1999), which separate it from the middle to upper crustal rocks of the Strona–Ceneri Zone (SCZ). The IVZ and the SCZ have been interpreted as a tilted section of continental crust that progressively exposes deeper rocks from the southeast to the northwest (e.g. Fountain 1976). Structural studies and interpretation of seismic data indicate that after considerable thinning during early Mesozoic rifting (Handy 1987; Bertotti *et al.* 1993), the IVZ was tilted during Alpine convergence. Tectonic disturbance related to Alpine collision is comparatively minor and most of the pre-Alpine geometries and structural relationships are well preserved (e.g. Schumacher 1997; Schmid *et al.* 1987).

The Balmuccia peridotite (Fig. 1) is the largest in a series of ultramafic bodies cropping out in the IVZ (Rivalenti *et al.* 1975; Shervais & Mukasa 1991; Quick *et al.* 1995). It is located just east to the ISZ and bordered by the mafic complex, a Permian lower crustal intrusion consisting of a sequence of ultramafic cumulates, gabbros and gabbro-norites grading eastwards into diorites (Rivalenti *et al.* 1981). The western margin of the Balmuccia peridotite is in tectonic contact with the gabbroic rocks of the mafic complex, while the eastern margin is an igneous contact with the basal series of the same complex, including cumulitic pyroxenites, peridotites and gabbros (Sinigoi *et al.* 1983; Shervais & Mukasa 1991). The mafic complex represents a deep-seated intrusion emplaced at depths of 25–30 km during the Permian (Rivalenti *et al.* 1984; Sinigoi *et al.* 1994; Peressini *et al.* 2007). Its emplacement caused heating and

partial melting of the lower crust made by gneisses of the kinzigite formation, which bound the eastern limit of the complex and are also found as septa included in the complex (Rivalenti *et al.* 1981; Sinigoi *et al.* 2011). Recent petrological and geochronological work demonstrated that the mafic complex in the IVZ and the granitic plutons, rhyolites and volcanic breccias of the southern SCZ are all part of the same magmatic system that emplaced in the crust between 286 and 281 Ma (Quick *et al.* 2009; Karakas *et al.* 2019).

The Valmala peridotites, for which scarcer data are available (Quick *et al.* 1995), are two smaller bodies (too small to be clearly visible in Fig. 1) that crop out in the vicinity of the homonymous valley, 2 km East of the village of Scopa (Fig. 1). They are bounded by pegmatitic clinopyroxenites and cumulus peridotites, which are in sharp contact with the gabbros of the mafic complex (Quick *et al.* 1995). The Balmuccia peridotite has been interpreted either as the top of a mantle section over which the mafic complex intruded in Permian times (Rivalenti *et al.* 1975, 1981; Shervais 1979), or as a lens of mantle rocks that have been mixed in an accretionary prism during Palaeozoic subduction processes (Quick *et al.* 1995). The latter scenario has been suggested also for the Valmala peridotites (Quick *et al.* 1995).

## 3 SEISMIC SURVEY AND DATA

In 2020, geophysical profiling was carried out to investigate the subsurface of the peridotites and gabbros in the region of Balmuccia (Piemonte region, NW-Italy). A controlled-source seismic experiment was conducted to derive a structural image for the first few kilometres at and around the location of the outcropping peridotite body (Fig. 2). Along two crossing profiles, one ∼11 km long, NNE-SSW and one ∼16 km, roughly E–W trending, investigations using reflection seismic method were accomplished. A fixed spread of 110 seismic recorders, equipped with short-period, vertical component sensors (4.5 Hz eigenfrequency), were permanently deployed along both seismic lines and spaced ∼250 m apart (Fig. 2). These receivers recorded Vibroseis source exited waves from 432 source points spaced roughly 60 m apart. The Vibroseis source signal was a linear frequency-modulated sweep with a frequency range from 10 to 110 Hz and 14 s duration. After pre-processing (Vibroseis correlation and vertical stacking) of source records, the data set consists of 110 receiver gathers from the 432 sources. Fig. 3 shows a typical example of two receiver gathers. The traveltime of first breaks (refracted *P*-wave phases) were then manually picked at all traces with sufficient signal-to-noise ratio, resulting in 24 392 traveltime picks. These picks were used to derive a shallow, upper crustal 3-D *P*-wave velocity model by tomographic methods. The actual experiment geometry, that is, the distribution of sources and receivers, was mainly designed to derive the 2-D structure of seismic reflectivity below the two seismic profiles. The recording of all seismic sources at all fixed stations (including fan-like observations) provided a data set suitable for 3-D interpretation. The geometry of the seismic experiment is not ideal for a full 3-D analysis, and the resulting tomographic images should not be overinterpreted. However, the use of a 3-D inversion (instead of 2-D) is particularly useful in case of significant deviations from the 2-D line geometry (crooked line) as in our data set, due to constraints by the high topography and steep relief (restricted accessibility for sources and receivers).
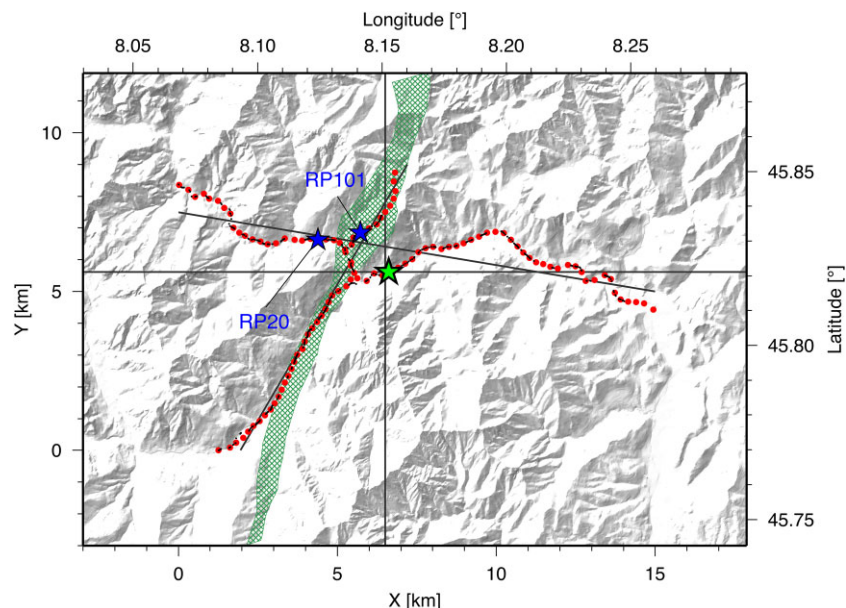
**Figure 2.** Topographic map showing the distribution of 110 receivers (red circles) and 432 seismic sources (black dots) covering the same area as in Fig. 1. The receivers recorded all sources from both seismic lines (fixed stations). For logistic reasons, the two lines followed mainly roads in the valleys. RP20 and RP101 (blue stars) are sensor locations for which data are shown later. Black lines indicate location of vertical slices in Figs 6–8, the green hatched area maps the ISZ and the green star marks the planned drilling location. The origin of the relative *X–Y* coordinate system is at 8.06796° E, 45.76976° N.

## 4 TRAVELTIME INVERSION METHOD

Instead of using a classical linearized traveltime inversion technique (with regularization including damping, smoothing and a starting model) we applied a tomographic inversion technique based on Bayesian statistical methods using a trans-dimensional, hierarchical Monte Carlo search with Markov chains using a Metropolis/Hastings sampler (Bodin *et al.* 2012) to derive the 3-D distribution of *P*-wave velocity, together with its uncertainty. This approach follows and extends the traveltime inversion technique presented by Ryberg & Haberland (2018). The Bayesian method combined with very wide (un-informative) prior information avoids the potentially subjective choice of starting velocity models, damping and smoothing parameters, and their (potential) influence on the final inversion result, as in classical inversion techniques. The traveltime calculations (solving the forward problem) for a given model are done by a fast finite-difference based Eikonal solver (*time3d*, Podvin & Lecomte 1991; Tryggvason & Bergmann 2006). The Eikonal solver, given its high computational speed, is essential when using the Markov chain Monte Carlo (McMC) inversion approach since the forward problem must be solved orders of magnitude more often compared to classical inversions. The 3-D seismic velocity field is discretized by a set of polyhedral Voronoi cells (described by cell centres), with a *P*-wave velocity value assigned to every cell; for details of the method see Bodin *et al.* (2012). The model misfit, that is, the differences between the traveltimes observed and predicted by the model, is calculated with the fast Eikonal solver for a given model. This is computationally challenging for the 3-D case and sufficiently finely sampled grids.

The Markov chains are started with a model consisting of a random number of Voronoi cells with random cell centres (uniformly distributed) and *P*-wave values, respectively. By randomly changing the model (changing the velocity and/or position of a cell, adding or removing a cell, details in Bodin *et al.* 2012) and evaluating the traveltime misfit we construct a Markov chain of consecutive models. After a burn-in phase (i.e. part of the Markov chain where the misfit

is still steadily decreasing), the (well-fitting) models are decimated (i.e. only every 20th model is selected from all well-fitting models) and then gathered for further derivation of a reference solution. We allow for a very wide range of *P*-wave velocities to be tested, including values not expected for typical rocks (0.1–10 km s$^{-1}$) to assure an unbiased sampling of the posterior *P*-wave distribution at any location in the 3-D model. For even more extensive model space exploration, models from 1000 separately evolving chains are investigated. The final results after the burn-in phase (several thousands of well-fitting models) are combined to analyse their statistical properties, that is, averages and uncertainty estimates at all locations in the 3-D model volume.

The inversion is trans-dimensional because the number of Voronoi cells is not fixed, treated as a variable instead, and it is hierarchical because we invert for data noise. Data noise is summarized as the remaining data misfit which cannot be explained by the model (i.e. the sum of true traveltime pick errors, forward calculation approximations, misidentified phases, errors introduced by anisotropic seismic velocity, etc.). This approach has the advantage that the derived models (distribution of velocities and their uncertainties) are almost completely data-driven. The trans-dimensional and hierarchical version of McMC method with Metropolis–Hastings proposals (Metropolis *et al.* 1953) is especially suitable for inversion of data set with poor geometry, that is, refraction seismic data sets with sources and receivers only at the surface and 2-D data sets with poor experiment geometries. In these cases, the McMC method automatically suppresses the potential development of imaging artefacts, by imaging fine-scale structures only where data availability permits, which is an advantage compared to classical, linearized inversion methods, where the final model might be significantly dependent on the choice of inversion parameters (i.e. starting model, damping and smoothing values).

Since the forward calculations are the main controlling factor with respect to the CPU time, combined with the requirement of a sufficiently fine forward grid to assure correct traveltime
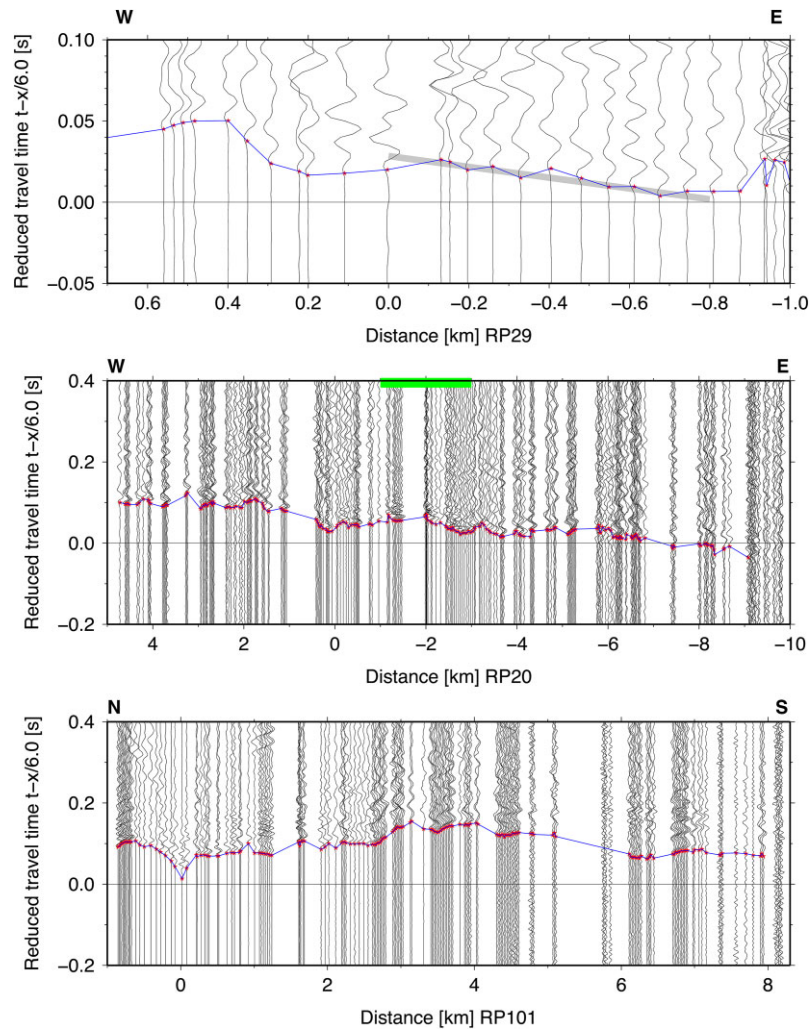
**Figure 3.** Three receiver gathers (location see blue and green stars in Fig. 2) showing typical data examples Vibroseis correlated data of all in-line sources (RP20 and RP 29—E-W line and RP101—N-S line). The unfiltered traces (raw data, traveltimes reduced by 6 km s$^{-1}$) are sorted according to observation distance and amplitudes are trace-normalized. The red stars indicate the manually determined arrival times of the refracted phases. The bottom diagram shows data from receiver point RP101 along the N-S line. The middle panel is from RP20 along the E-W line, the location of the ISZ and its extent is shown as thick green line. The top panel shows a zoom-in of the data from a receiver gather at the proposed borehole location (green star in Fig. 2) crossing the peridotite body. The near-offset first arrivals show a high apparent velocity (thick grey line corresponds to 7.5 km s$^{-1}$) indicative for the presence of a shallow, high-velocity body.

calculations (the Eikonal solver CPU-time depends approximately on the grid size), we decided for an iterative approach. The final forward grid size of 62.5 m the inversion was not feasible directly, so we decided to start the Markov chains with a sparser forward grid size (500 m) and after 2000 models, when the misfit became stable, to decrease the grid size by a factor of 2. Again, after each 2000 models we decreased the grid size further (Fig. S4, Supporting Information). From model number 6000 to 8000, we reached the final grid size of 62.5 m. We are aware that this changing of the forward calculations is subjective, however it dramatically reduces the computation time, and inversions going from coarser to finer grids are not uncommon in seismology (e.g. Hetényi *et al.* 2011).

Fig. 4 shows the evolution of 1000 Markov chains, both for misfit and model complexity (number of Voronoi cells). It shows the steady decrease of misfit and increase of model complexity. The final burn-in phase was assumed to be reached for models with numbers > 7000. All models beyond 7000 have been analysed (calculations of averages and uncertainty estimates at every location

in the 3-D model volume) to derive a final 3-D *P*-wave velocity model.

## 5 BALMUCCIA 3-D VELOCITY MODEL

The resulting 3-D model is presented in Fig. 5 (map views), 6 (West–East and South–North depth sections), 7 (depth section along the West–East profile) and 8 (depth section along the South–North profile). In all these figures, the seismic *P* velocity (average of all derived models after the burn-in phase) as well as the corresponding uncertainty (standard deviations of all models after the burn-in phase) are colour-coded.

As expected for tomographic inversions using data acquired at the surface, the uncertainties (standard deviations) are smaller close to the surface (typically between 0.1 and 0.7 km s$^{-1}$) and increase with depth. A threshold uncertainty of 1.2 km s$^{-1}$ is assumed to indicate the limit of well resolved regions. The areas of the velocity model exceeding this uncertainty threshold are shown in faded colours.
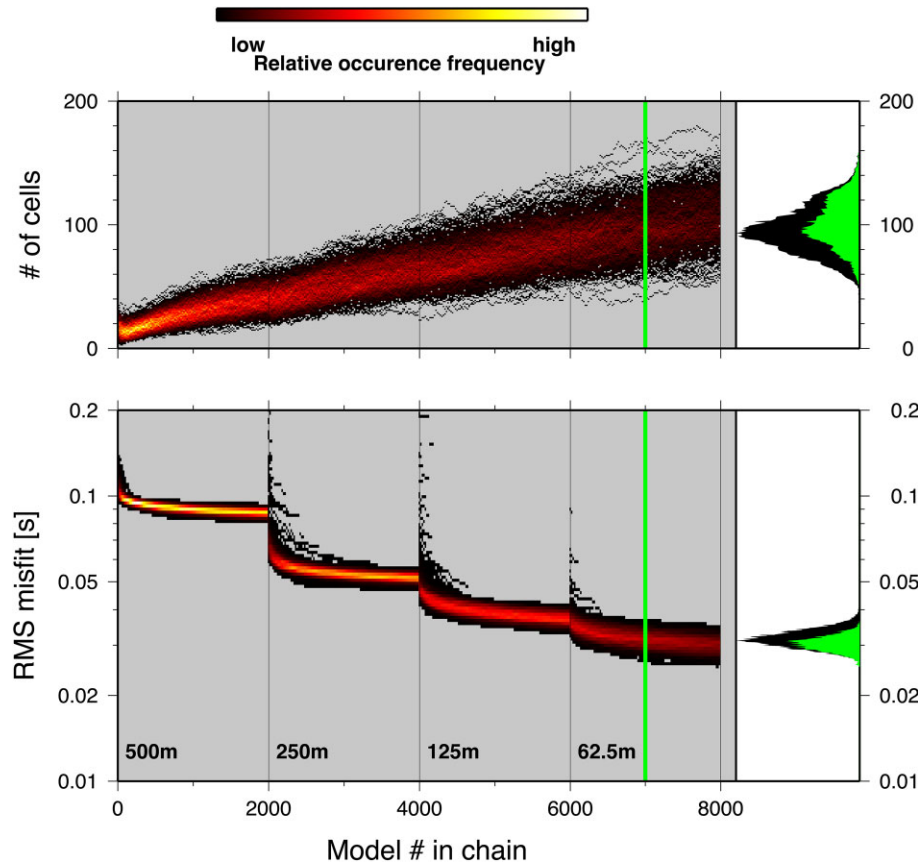
**Figure 4.** Evolution of misfit along Markov chains. Shown is the histogram distribution of the data misfit in seconds (bottom) and the model dimension (number of cells, top) during the evolution along 1000 Markov chains (see the text for details) using a heat-map colour scale (with black–red–yellow–white indicating progressively increased frequency). The black lines at 2000, 4000, 6000 and 8000 indicate the change of forward model grid size (decreased by 2 at every line, forward grid size in metres is indicated). Relative histogram plots of the distribution of data misfit (bottom) and model dimension (top) are added at the right-hand side, with all models of the last inversion phase shown in black, green models are the 90 per cent best-fitting models of post burn-in phase (model number after green vertical line). The best-fitting models (green) are typically characterized by higher model dimensionality. The forward problem (traveltime calculations) was solved for more than $3.5 \times 10^7$ models. Note the log scale for the data misfit.

This limit is reached at a maximum depth of 3 km below mean sea-level (MSL, corresponding to approximately 4 km below surface) in the centre of the study area. However, depending on the source–receiver geometry and the seismic velocity distribution, the depth of well-resolved zone is not uniform and varies throughout the model. Accordingly, some regions of the model are only well resolved down to a depth of 1 km MSL. An in-depth discussion of the uncertainties is given in the Supporting Information (Figs S1–S3).

Seismic *P*-wave velocities imaged by our survey range from 4.5 to 7.5 km s$^{-1}$, with an expected general trend of increasing velocities with depth (Fig. 9), see examples of posterior velocity distribution in well and poorly imaged regions (Figs S1 and S3, Supporting Information). The map view of $V_p$ close to the surface (Fig. 5, top left) correlates well with the surface geology (Fig. 1). A sharp velocity change from slow $V_p$ in the West to high $V_p$ in the East occurs at the ISZ. The most prominent feature of the model is the peaked or ridge-like structure of high seismic velocities (i.e. >6 km s$^{-1}$) reaching the surface in the centre of the model. The centre of this protruding structure is located slightly East of the village of Balmuccia, coincident with the geologically mapped peridotite outcrop, and runs in south-westerly direction, where the 6 km s$^{-1}$ velocity isoline reaches the surface (see Figs 5–9). To the West much lower velocities are found down to 1 and 2 km depth, and also to the East lower velocities can be noted. The transitions

from this protruding structure to the surrounding regions (to the West and the East) are sharp gradients (strongest to the West down to 1 km depth below topography, see upper right panel of Fig. 7) suggesting a rather abrupt contrast between different lithological units. The transition to the West corresponds to the ISZ (Fig. 9). The largest gradients, which typically occur at interfaces, are found at velocities of ~6 km s$^{-1}$ (Fig. 9). This contour is then interpreted as proxy for an interface/boundary and shown with a black line in Figs 5–8 and in the Supporting Information. Towards greater depth, the 6 km s$^{-1}$ velocity isoline does not close on itself but widens, hence representing larger volumes of high-velocity rocks.

Synthetic tests (see Fig. S2, Supporting Information) with different geometries show that the shape of the protruding feature is well resolved down to a depth of ca. 1 km MSL, and that there is no sign of a downward narrowing body.

## 6 DISCUSSION

The 3-D tomography model reveals a high-velocity body ($V_p$ > 6 km s$^{-1}$) whose boundaries are well delineated by high values of the velocity gradient (Figs 5–9). The high-velocity body is shaped as a pointy body whose peak reaches the surface East of Balmuccia village at the outcropping peridotite body and broadens
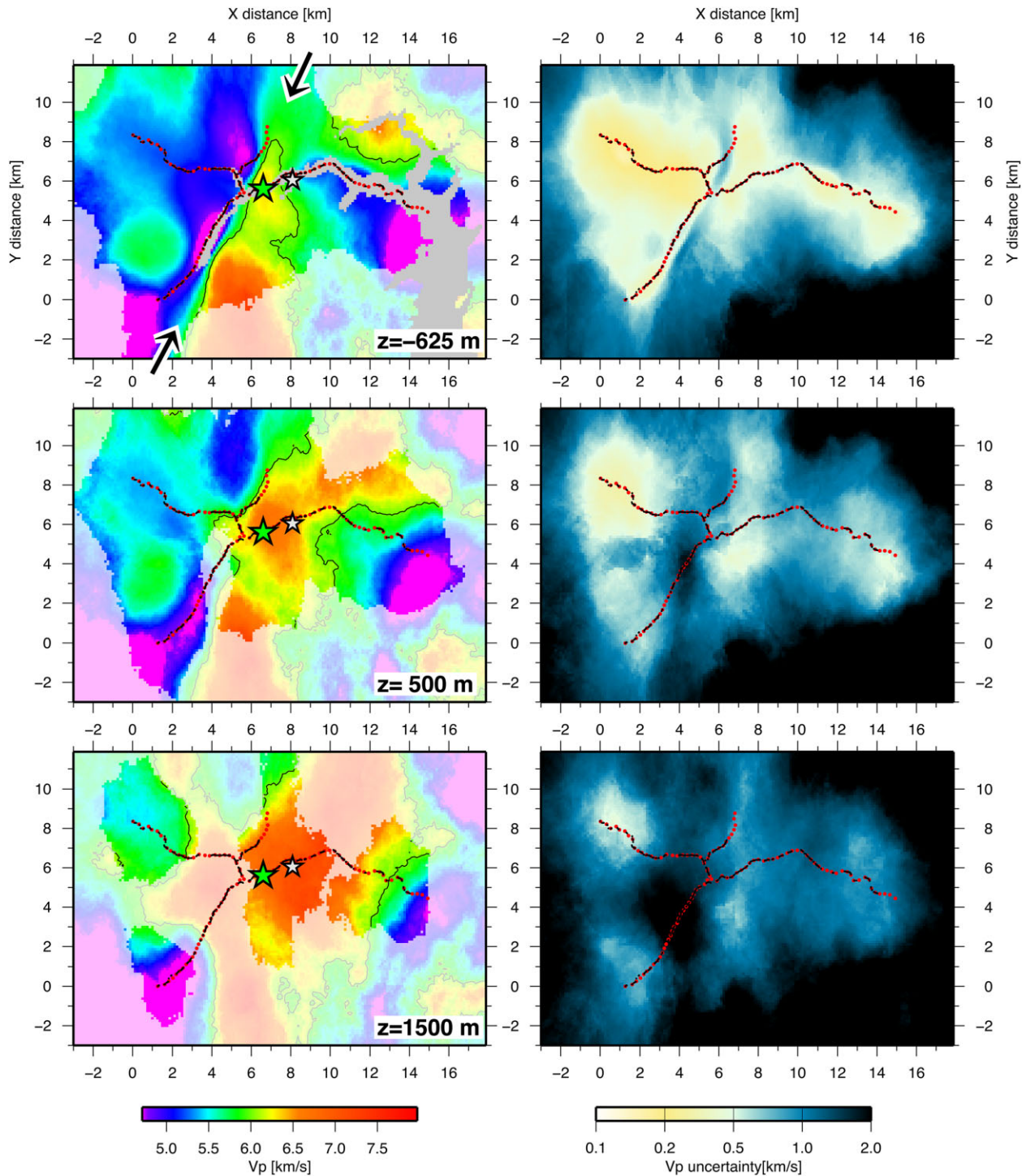
**Figure 5.** Horizontal cross-sections through the 3-D *P*-wave velocity model (left) at −625, 500 and 1500 m depth (0 is MSL), shown with the 6 km s⁻¹ velocity isoline (black line), sources and receivers for orientation (red/black dots), the planned drilling location (green star) and an alternate drilling site (light grey star). The black arrows in the uppermost depth slice mark the location of the ISZ. Grey areas in the −625 m depth slice indicate regions above topography, less saturated colours in all velocity slices show regions of higher velocity uncertainty (>1.2 km s⁻¹). Right corresponding velocity uncertainties at the three depth levels. Small uncertainties are found mainly at shallower depths (light colours). The uncertainties quickly increase with depth, a typical observation for refraction style observations with sources and receivers located at the Earth's surface.

downwards. The body continues down to the bottom of the tomography model (∼5 km depth MSL), but only areas with a low level of $V_p$ uncertainty (<1.2 km s⁻¹) are interpreted here. However, caution is needed in these areas as well, see, for example, depth slice at −625 m MSL in Fig. 5: (1) not all areas with moderate

uncertainty can be interpreted, for example, the outer areas of the velocity model. There, larger Voronoi cells are used (automatically) to balance the low data coverage resulting in apparent moderate uncertainty values, but due to these larger cells (500 m and more) the spatial resolution is lower in these areas. (2) Not all areas with higher
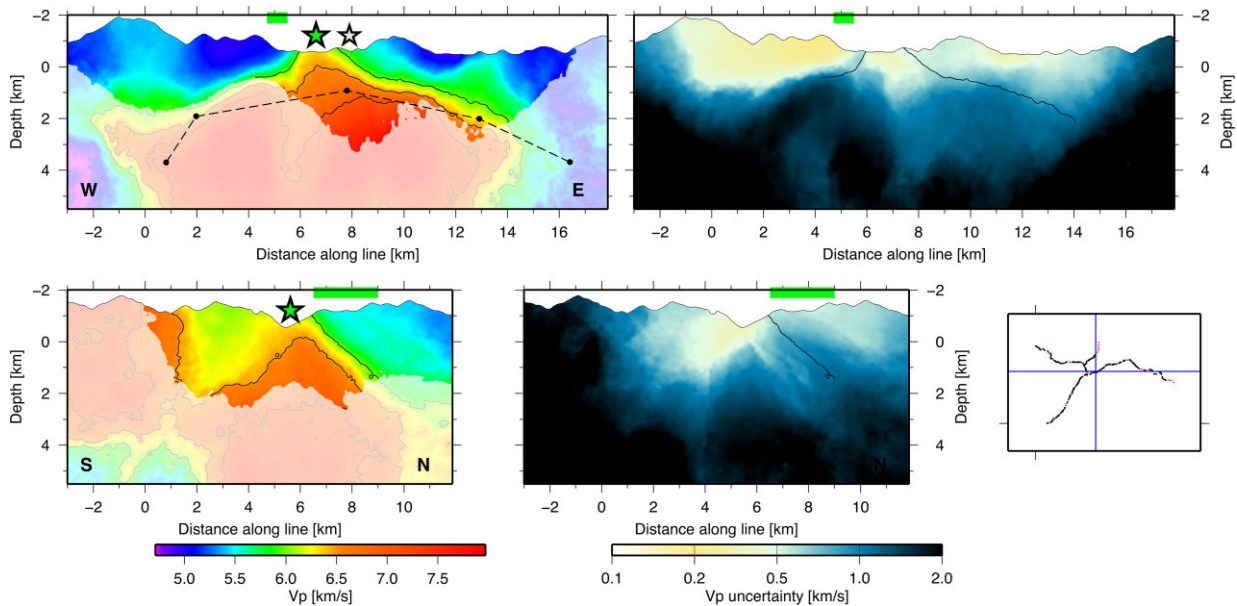
**Figure 6.** N-S and W-E vertical cross-sections through the 3-D *P*-wave velocity model (left) and their uncertainty (right). The resolution is good down to several kilometres depth (yellow to light-blue colours in the right-hand panels, reported as shading on the left at $> 1.2$ km s$^{-1}$ uncertainty). For reference, the 6 km s$^{-1}$ velocity isoline (black line) is shown in all sections (see also Fig. 5) and velocity isolines of 6.5 and 7 km s$^{-1}$ are additionally shown in the $V_p$ model. The planned drilling location is marked as green star and an alternative drilling site is marked as light grey star. The location and extent of the ISZ is marked as thick green line at the top of the figure. Bottom right shows the location of the cross-section with respect to the sources and receivers (black and red dots, respectively). The dashed–dotted black line in the W-E section illustrates the top of the IGB (Scarponi *et al.* 2020) ∼3 km North of the profile.

uncertainty are poorly resolved, for example, the central part of the model (Fig. 5 depth slice at −625 m MSL). The area with small uncertainties (high-velocity resolution) is intersected by a band of high uncertainty trending from SW to NE. These higher uncertainty values are located at the western margin of the high-velocity body, where a strong horizontal velocity contrast exists. It is typical for McMC inversions that sharp velocity contrasts are surrounded by halos (or ghosts) of higher uncertainty ('loops of uncertainty', see Galetti *et al.* 2015). The 2-D recovery tests show that although the recovery accuracy decreases with depth, the general shape and magnitude of the pre-defined anomalies could be recovered well down to a depth of generally 1 km MSL which is approximately 2 km below the surface (see Fig. S2, Supporting Information). The recovery of the asymmetric shape of the high-$V_p$ body with a steeper flank in the West (the ISZ) compared to the East (Fig. 7) was also successful and is a robust observation. This is in very good agreement with the 3-D gravity and the 2-D joint gravity-seismology inversion analyses (Scarponi *et al.* 2020, 2021) which also revealed an asymmetric shape of the anomalous body in the crust, reaching very close to the surface.

The location of the high-$V_p$ body ($V_p > 6$ km s$^{-1}$, Figs 5–9) is in good agreement with the location of the surface outcrop of the Balmuccia peridotite (Fig. 1; Quick *et al.* 2003; Piana *et al.* 2017a,b). In the southern part of the Balmuccia peridotite the 6 km s$^{-1}$ $V_p$-isoline (representing a proxy to an interface/boundary) reaches the surface as well. In contrast to the surface geology, the 6 km s$^{-1}$ $V_p$-isoline/interface descends towards North, which is presumably an artefact due to the acquisition geometry. Since only large offset data are available in this area, the *P* waves propagate at greater depths resulting in lower data coverage (resolution) at the surface. At the western border of the high-$V_p$ body, where the 6 km s$^{-1}$ isoline/interface shows a dip of ∼60° down to 2 km depth MSL, we observe a very sharp velocity change (strongest $V_p$ gradients measured) where the ISZ is located (Fig. 1). Considering the range

of possible dips in the $V_p$-gradient profile (Fig. 7, right), leaving room for 60°±25° dip, this observation fits well with the geologically observed dips of the ISZ, that are generally 85° to the West. For more accurate imaging of steeply dipping structures, dedicated seismic processing workflows are needed, as presented in the previous seismic survey (Liu *et al.* 2021). However, their profiles were not long enough to image structures below 1 km. An open question is the downdip geometry of the ISZ. It was proposed that this fault continues at high angle to large depths (up to >20 km, Schmid *et al.* 2017). The 6.0 km s$^{-1}$ $V_p$-isoline and the $V_p$-gradient (Fig. 7) suggest a steep dipping fault down to 1 km depth MSL. However, below 1 km depth MSL, the ISZ geometry cannot be determined robustly since the uncertainty of our seismic results increases significantly. Thus, the shallower dip at 2 km depth MSL cannot be confirmed. Towards the South, the Balmuccia peridotite is not visible at the surface and overlain by gabbro (Quick *et al.* 2003). In the southernmost part of the study area, approx. 2 km East of the village of Scopa (Fig. 1), small peridotite outcrops of the Valmala peridotite are mapped (Quick *et al.* 2003) that might indicate only a shallow depth of the peridotite in this region. This may correspond to a second structural high in the high-$V_p$ body that is located close to the surface (Fig. 5; $x = 5$ km and $y = 1$ km) and shows the ability of semi-3-D active seismic surveys to resolve finer scale structures than 3-D, few-km scale gravimetry (Scarponi *et al.* 2020). Towards East, the boundary of the high-$V_p$ body is characterized by a gently eastward dip and significantly lower $V_p$ gradients indicating a smoother transition from the peridotite body to the mafic complex. This, indeed, could represent an original lower crust–mantle transition, with a spatial transition on the order of few to several hundreds of metres (see James *et al.* 2003 for a cratonic example and Scarponi *et al.* 2021 for the local analysis co-located with our survey).

The high-$V_p$ body with velocities from 6 up to 7.5 km s$^{-1}$ is interpreted as mantle material and might represent the continuation of the Balmuccia and Valmala peridotites at depth. Laboratory analysis
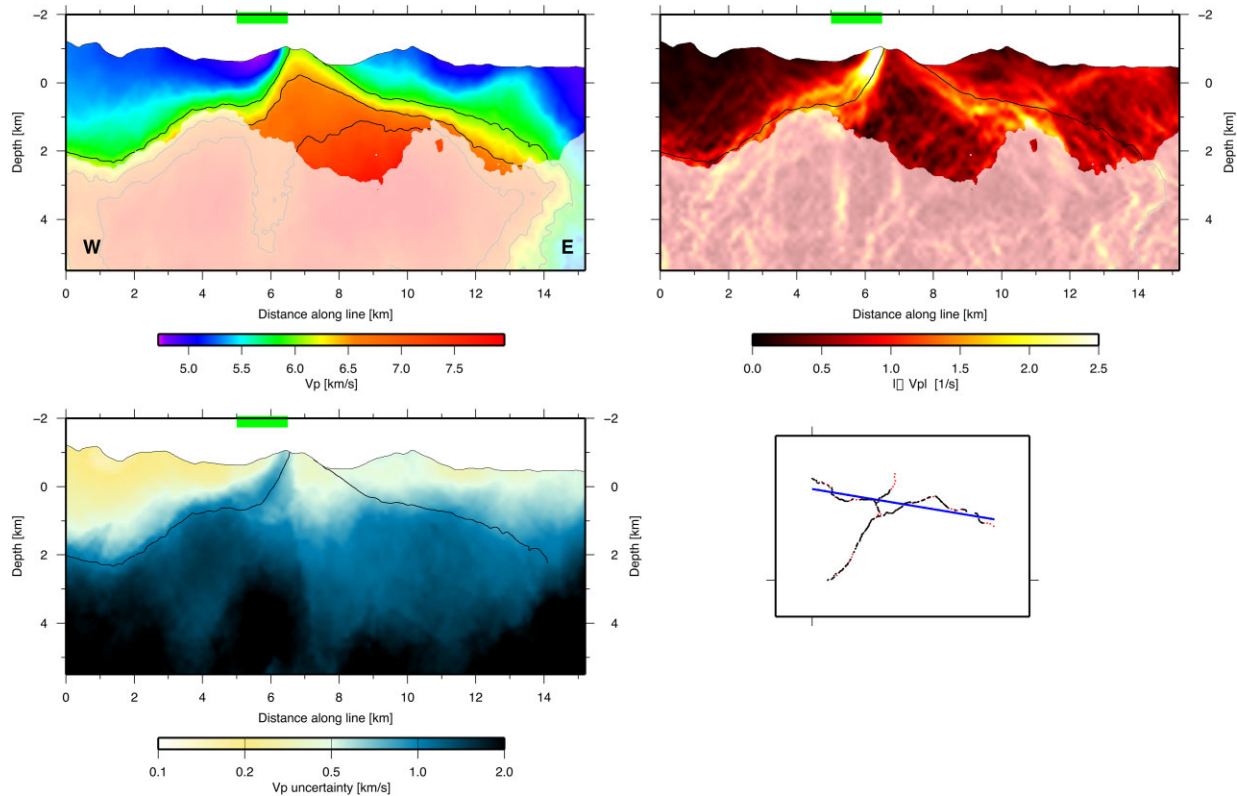
**Figure 7.** Vertical cross-section of *P*-wave velocity (top left) roughly along the W-E seismic line with corresponding uncertainty (bottom left). This profile crosses the Balmuccia peridotite roughly 1 km north of that shown in Fig. 6. The cross-section shows an asymmetric, high-velocity body, outcropping in the central part. Regions of large velocity uncertainty (low resolution) are shown with low colour saturation. The 6 km s$^{-1}$ velocity isoline (black line) is shown in all sections for reference and the $V_p$ model is additionally overlain by 6.5 and km s$^{-1}$ velocity isolines. Top right shows the distribution of the absolute value of the 3-D velocity gradient, indicative for potential velocity (rock) boundaries, saturated colours concentrate on well resolved (low uncertainty) regions. Bottom right shows the location of the cross-section with respect to the sources and receivers (black and red dots, respectively). The location and extent of the ISZ is shown as thick green line.

of peridotite samples showed even higher velocity values of 7.8–8.1 km s$^{-1}$ (e.g. Burke & Fountain 1990; Khazanehdari *et al.* 2000; Vilhelm *et al.* 2008) and thermodynamic calculations based on rock compositions of the Balmuccia peridotite confirmed the viability of these values at 3 km depth (Pistone *et al.* 2020). However, partial serpentinization (5–35 per cent) of harzburgite could decrease the velocity from 8 to 7 km s$^{-1}$ (Escartin *et al.* 2001). A *P*-wave velocity reduction to 7.5–6.7 km s$^{-1}$ was derived for a serpentine content of 20–45 per cent correlating with densities of ~3.0–3.2 g cm$^{-3}$. However, the Balmuccia peridotite is extremely fresh with overall less than 5 per cent serpentinization. Another study (Vilhelm *et al.* 2008) conducted *in-situ* seismic measurements at the surface of the Balmuccia peridotite, revealed a slower average velocity of 6 km s$^{-1}$. Their laboratory analysis of the peridotite samples which were performed under atmospheric pressure showed high seismic velocity of ~7.7 km s$^{-1}$. We assume that the small samples (~5–10 mm) analysed in the lab most likely show the property of the undisturbed rock. The field measurements determine the rock properties at a larger scale (here 10 m) and the rocks are then affected by micro/macroscopic faults/cracks or weathering effects. There are several generations of peridotite mylonite, cataclasite and pseudo-tachylite cutting the peridotites (e.g. Souquière & Fabbri 2010; Ueda *et al.* 2020) that along with serpentinized fractures could lower $V_p$ of the Balmuccia peridotite near the surface. These fractures, albeit usually less than 10 cm thick, are likely to continue at depth and they could contribute to seismic velocity reduction. The

Balmuccia peridotite is also crosscut by dykes and veins of pyroxenites and gabbronorites (Sinigoi *et al.* 1983; Shervais & Mukasa 1991; Mazzucchelli *et al.* 2009), which might also slightly decrease $V_p$ at larger scale. Overall, the measured seismic velocities of the high-$V_p$ body which increase from 6 km s$^{-1}$ at the surface to 7.5 km s$^{-1}$ at depth of ~3 km (Fig. 9) are generally in good agreement with the lab and small-scale field measurements of Balmuccia peridotite.

Considering the good agreement of the high-$V_p$ body and the Balmuccia peridotite body in both surface location and seismic velocity, our high-$V_p$ body is interpreted as the seismic image of the Balmuccia peridotite. The shape of the Balmuccia peridotite as well as the Valmala peridotite was extrapolated from geological observations and was depicted as isolated bodies (lenses) with a vertical extension of ~1.5 to 2 km (Quick *et al.* 2003) and no connection to the underlying IGB (Berckhemer 1968; Diehl *et al.* 2009). In contrast to that, we recovered a pointy high-$V_p$ body that broadens downwards and continues down to a depth of at least ~3 km MSL. Several large-scale models developed from gravity or seismological data suggest an eastward inclined high-density, high-velocity body that extends down to the mantle but starting at variable depths (Berckhemer 1968; Diehl *et al.* 2009; Scarponi *et al.* 2020, 2021). A vertical W-E section through the 3-D model of Diehl *et al.* (2009) presents a high-velocity body ($V_p > 6$ km s$^{-1}$) at ~6 km depth MSL below Balmuccia, increasing eastwards to 7 km s$^{-1}$ at 18–20 km depth MSL ~20 km East of Balmuccia. Since the spatial resolution
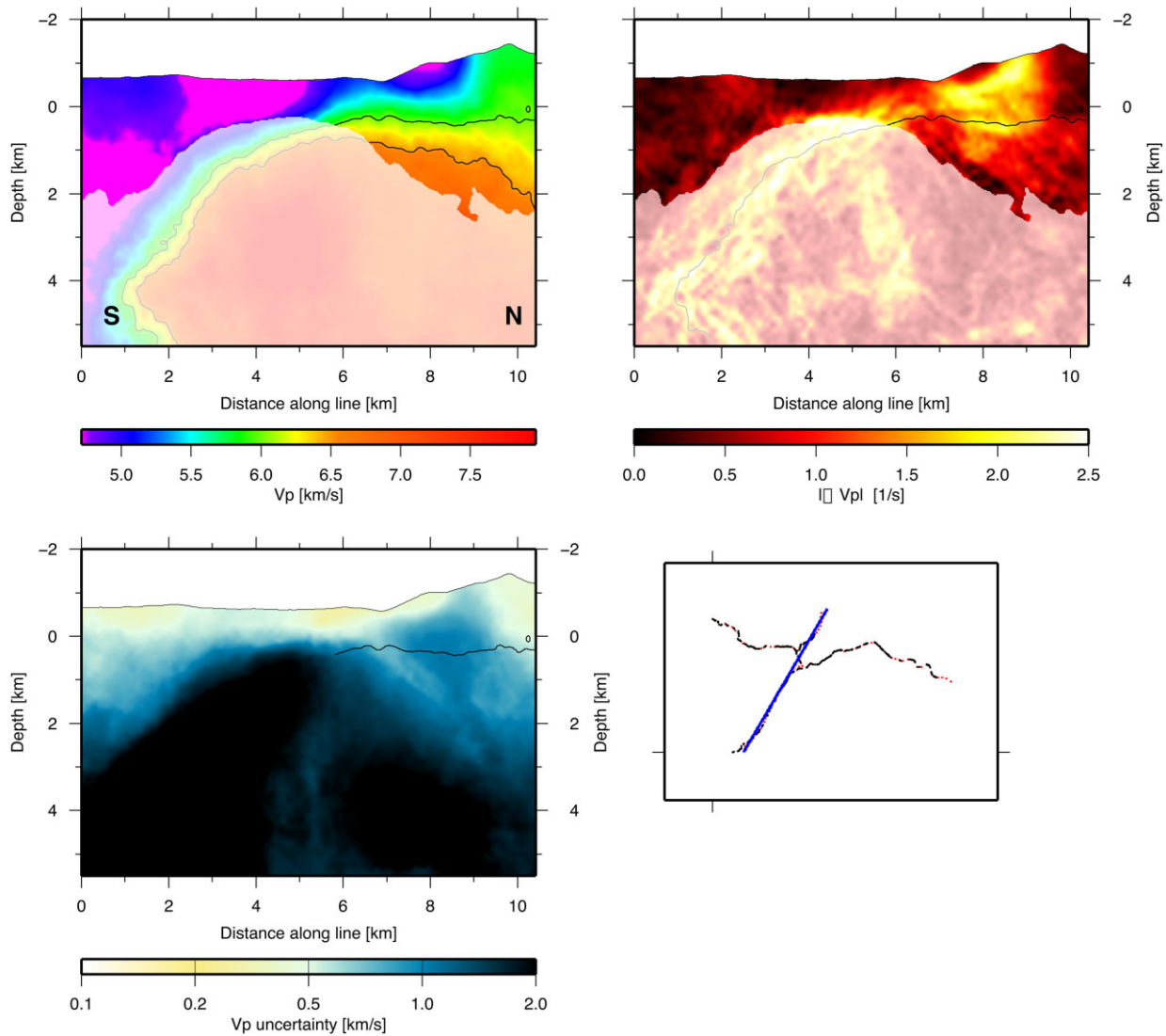
**Figure 8.** Same as Fig. 7: vertical cross-section along the S-N seismic line that runs along the ISZ. The 6 km s$^{-1}$ velocity isoline is shown in all sections for reference, while the 6.5 km s$^{-1}$ velocity isoline is added in the $V_p$ model. The southern part of the profile is characterized by low velocities ($<5.3$ km s$^{-1}$). As above, indications of the high-velocity body in the northern part of the line, not reaching the surface, can be seen.

of that study is rather coarse (25 km × 25 km × 15 km grid), this model was not designed to recover small-scale $V_p$ changes. Therefore, a direct comparison with our small-scale model is difficult. Nonetheless, we observe $V_p > 6$ km s$^{-1}$ much closer to the surface than Diehl *et al.* (2009). New gravity data (Scarponi *et al.* 2020) that cover the area of Balmuccia present the 3-D structure of the IGB. It reaches the shallow subsurface (1±1 km depth MSL dependent on the assumed density contrast) and is wider than proposed by previous studies. The density contrasts used in their analyses (300–500 kg m$^{-3}$) indicated that the IGB is composed of ultramafic rock and mantle peridotites. The asymmetrical shape of the IGB close to the surface is revealed by a joint gravity-seismology inversion analysis (Scarponi *et al.* 2021). The western flank is steeply dipping, the eastern flank is gently-dipping and in between a shallow local peak (1–3 km MSL) is visible. The better resolved high-$V_p$ body derived in our study has an asymmetrical shape with a peak. This peak is too small to be recovered by the density model/gravity data. The lower and broadened part of our high-$V_p$ body correlates well

with the wider top of the first IGB model (Scarponi *et al.* 2020; Fig. 6), considering the lateral distance between both W-E-sections (~3 km between density and seismic line) and that the modelled depth of the IGB is dependent on the density contrast used. This might indicate that the Balmuccia and Valmala peridotites represent the surface expression of the IGB and are connected at depth. The depth resolution of Scarponi *et al.* (2020) was lower due to the methods employed, but our new results combined with those of Scarponi *et al.* (2020) establishes a continuity of geophysical anomalies in the current upper crust. This would imply that (i) a portion of the uppermost subcontinental mantle beneath the western Southern Alps crops out at the surface and (ii) this portion is in igneous contact with the lower crustal lithologies of the IVZ on the surface. This supports the hypothesis that the contact between the Balmuccia peridotite and the layered series of the mafic complex might represent a fossil continental crust–mantle transition zone (Rivalenti *et al.* 1975, 1981; Shervais 1979). The results presented in this work thus question interpretations that the ultramafic
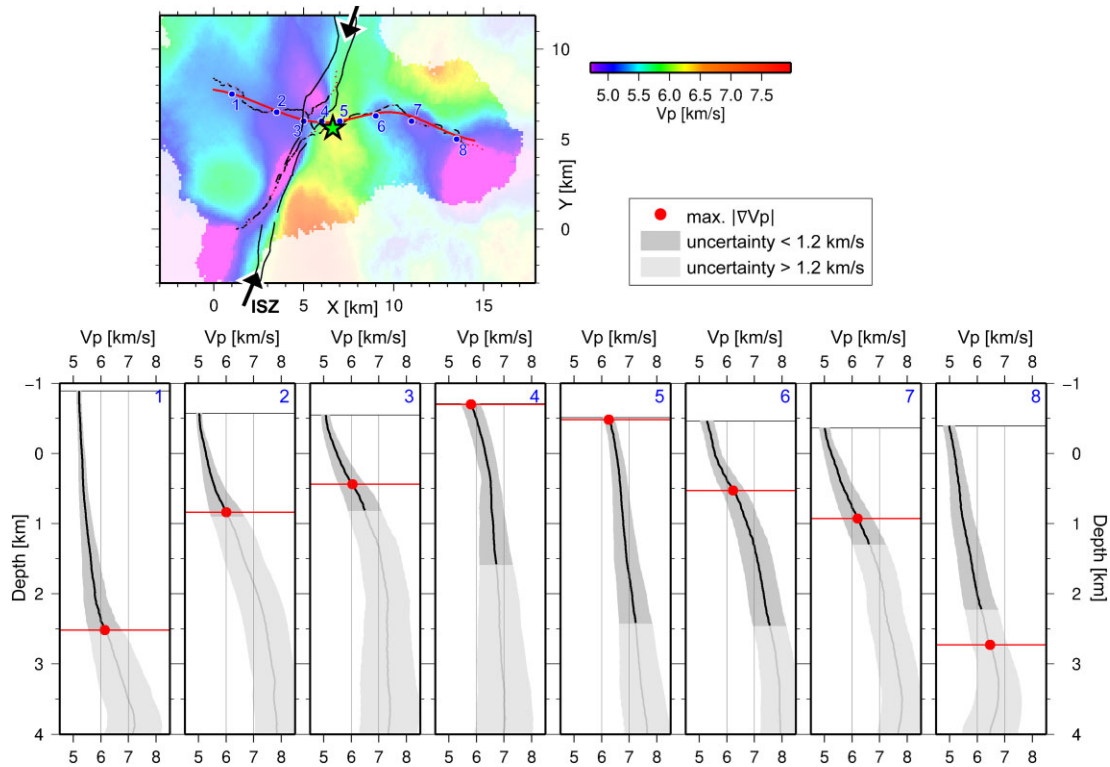
**Figure 9.** Horizontal section showing the *P*-wave velocity at the surface (top) and individual velocity depth functions (bottom) whose locations are marked with blue numbers. The $V_p(z)$ functions are shown as black solid lines overlaying the corresponding uncertainty (grey area) which increases with increasing depth. The maximum velocity gradients are marked as red dots and are typically found at velocities of ~6 km s$^{-1}$. The planned drilling location is shown in the horizontal section (green star).

bodies in the IVZ are fragments of mantle peridotites interfingered in the crust during pre-Permian accretionary processes (Quick *et al.* 1995).

Lab and field measurements show that some of the IVZ rocks have an anisotropic behaviour due to preferred orientation of minerals or microcracks and faults. In fact, the Balmuccia peridotite and the gabbros of the mafic complex are characterized by well-defined banding and mineral lineation, which are broadly N-S oriented (Shervais & Mukasa 1991; Quick *et al.* 1992). Khazanehdari *et al.* (2000) determined a seismic anisotropy coefficient *k* (Birch 1961) of ~4.4 per cent for ultramafic rocks (Balmuccia peridotite), 2.3–2.6 per cent for meta-igneous intrusive rocks (dunite and gabbrodiorite) and 3.5–7.8 per cent for metasedimentary rocks, whereby the anisotropy of amphibolite (7.8 per cent) is higher than for stronalite (gneiss) and kinzigite (schist). Vilhelm *et al.* (2008) performed lab analyses of peridotite samples from the Balmuccia peridotite and found an anisotropy coefficient of ~6 per cent. However, their lab measurements of the samples normal and parallel to the outcrop surface under atmospheric pressure shows only a value of 1.4 per cent. This is significantly smaller than the field-derived seismic anisotropy of ~25 per cent which was associated to weathering effects of the rocks or macroscopic and microscopic faults. This large anisotropy is probably not representative for most of the subsurface but rather restricted to the shallowest parts of the Balmuccia peridotite.

Although (moderate) anisotropy related to different mechanisms and of different amplitude could be expected in the subsurface, anisotropy was not included in the inversion model, for several reasons: due to the limited geometry, the data quality is not sufficient for the large number of (inversion) parameters required for

modelling seismic anisotropy. In addition, the 3-D McMC inversion is time-consuming. In our application without accounting for anisotropy, the inversion ran on a high-performance computing cluster (500 CPUs) and still required a computation time of ca. 100 d. By implementing anisotropy, the computation time would increase drastically, and given the data quality, consideration of seismic anisotropy in 3-D within the McMC concept is presently not feasible. In 2-D, seismic anisotropy could be implemented by assuming a vertically anisotropic medium VTI (vertical transverse isotropy). Without borehole information, however, this assumption is speculative in light of the design of the seismic experiment (surface sources and receivers only, no subsurface sources and receivers). Another issue is the wave propagation itself. The data were acquired in a rather difficult terrain (along crooked lines, in deep mountain valleys) resulting in complex and unconventional wave propagation, for example, from the valley upwards inside the mountain. Since such wave paths deviate from the propagation direction used in conventional refraction tomography, a 2-D approximation of seismic anisotropy is at present not feasible. Finally, even if a few per cent anisotropy could be constrained, compared to the significant $V_p$ variations, it would not affect the structural interpretation our results significantly (for analysis of post-inversion data misfits with respect to potential anisotropy, see Fig. S5, Supporting Information).

In the framework of the ICDP drilling project DIVE (Pistone *et al.* 2017) the original planning comprised to start drilling at the surface of the peridotite outcrop in a former quarry, and to continue drilling at a low to moderately high (10°–30°) angle from vertical towards the W-SW (cf. Figs 5 and 6, top-left panel, green star). Given the new results of this study, a more promising plan is to locate the drilling site near the village of Isola (cf. Figs 5 and 6,

top-left panel, light grey star), that is, starting in the lower crust and penetrating into mantle rocks to allow a smoother gradient from the mafic complex to the peridotite to be sampled. The final drilling scenario will be selected after evaluating and compiling the results from geophysical investigations (tomography, reflection seismics and local 3-D gravity) and geological field investigations of outcropping structures.

## 7  SUMMARY AND CONCLUSION

A controlled source seismic survey was carried out in the Balmuccia area to map the 3-D structure of the IGB in the shallow subsurface down to 3 km depth. By applying an inversion approach based on Bayesian statistical method using Monte Carlo search with Markov chains, a 3-D *P*-wave velocity ($V_p$) model was recovered. The resulting 3-D velocity model reveals a high-velocity body ($V_p$ >6–7.5 km s$^{-1}$) that stretches from the near surface down to 3 km depth and is interpreted as the Balmuccia peridotite. Towards the West, the body is limited by the steeply dipping ISZ, which is characterized by a sharp velocity change. In contrast to geological interpretations, we do not observe an isolated body, but rather a downward broadening body, thereby connected to the larger scale, high-density and high-velocity IGB imaged by Scarponi *et al.* (2020, 2021), and in lower resolution by Berckhemer (1968), Kissling (1984) and Diehl *et al.* (2009) spanning across the crust.

Since the inversion technique used operates without a pre-defined initial model, its result is not affected by *a priori* assumptions or hypotheses on expected structures. Thus, this independently derived high-spatial resolution tomographic image of the Ivrea body provides new and important details of the shallow subsurface that form a solid basis for the preparation of a deep drill hole of the ICDP drilling project DIVE. The results of SEIZE might ultimately provide a guide how to drill the crust–mantle boundary/transition structure across scales and sample its physics and chemistry variations.

## ACKNOWLEDGMENTS

## DATA AVAILABILITY

Data are archived at the GIPP Experiment and Data archive (https://doi.org/10.5880/GIPP.202016.2).

## REFERENCES

Artemieva, I.M. & Shulgin, A., 2019. Making and altering the crust: a global perspective on crustal structure and evolution. *Earth planet. Sci. Lett.,* **512,** 8–16.

Ashwal, L.D., Morgan, P., Kelley, S.A. & Percival, J.A., 1987. Heat production in an Archean crustal profile and implications for heat flow and mobilization of heat-producing elements. *Earth planet. Sci. Lett.,* **85,** 439–450.

Behn, M.D. & Kelemen, P.B., 2006. Stability of arc lower crust: insights from the Talkeetna arc section, south central Alaska, and the seismic structure of modern arcs. *J. geophys. Res.,* **111,** B11207. doi:10.1029/2006JB004327.

Berckhemer, H., 1968. Topographie des "Ivrea-Körpers" abgeleitet aus seismischen und gravimetrischen Daten. *Schweiz. Mineral. Petrogr. Mitt.,* **48**(1), 235–246.

Bertotti, G., Picotti, V., Bernoulli, D. & Castellarin, A., 1993. From rifting to drifting: tectonic evolution of the South-Alpine upper crust from the Triassic to the Early Cretaceous. *Sediment. Geol.,* **86,** 53–76.

Birch, F., 1961. The velocity of compressional waves in rocks to 10 kilobars, Part II. *J. geophys. Res.,* **66,** 2199–2224.

Bodin, T., Sambridge, M., Rawlinson, N. & Arroucau, P., 2012. Transdimensional tomography with unknown data noise. *Geophys. J. Int.,* **189,** 1536–1556.

Bois, C., Pinet, B. & Roure, F., 1989. Dating lower crustal features in France and adjacent areas from deep seismic profiles. in *Properties and Processes of Earth's Lower Crust*. AGU, Washington DC, pp. 17–31.

Boriani, A. & Sacchi, R., 1973. Geology of the junction between the Ivrea-Verbano and strona-Ceneri Zones (southern Alps). in *Memorie degli Istituti di geologia e mineralogia dell'Università di Padova,* Vol. **28**. Padova, pp. 1–36.

Burke, M.M. & Fountain, D.M., 1990. Seismic properties of rocks from an exposure of extended continental crust - new laboratory measurements from the Ivrea Zone. *Tectonophysics,* **182,** 119–146.

Christensen, N.I. & Mooney, W.D., 1995. Seismic velocity structure and composition of the continental crust: a global view. *J. geophys. Res.,* **100**(B6), 9761–9788.

Chroston, P.N. & Simmons, G., 1989. Seismic velocities from the Kohistan Volcanic Arc, northern Pakistan. *J. geol. Soc.,* **146,** 971–979.

Decarlis, A., Beltrando, M., Manatschal, G., Ferrando, S. & Carosi, R., 2017. Architecture of the distal Piedmont-Ligurian rifted margin in NW Italy: hints for a flip of the rift system polarity. *Tectonics,* **36,** 2388–2406.

Diehl, T., Husen, S., Kissling, E. & Deichmann, N., 2009. High-resolution 3-D P-wave model of the Alpine crust. *Geophys. J. Int.,* **179**(2), 1133–1147.

Escartin, J., Hirth, G. & Evans, B., 2001. Strength of slightly serpentinized peridotites: implications for the tectonics of oceanic lithosphere. *Geology,* **29,** 1023–1026.

Fountain, D.M., 1976. The Ivrea-Verbano and Strona-Ceneri Zones, northern Italy: a cross-section of the continental crust – New evidence from seismic velocities of rock samples. *Tectonophysics,* **33,** 145–165.

Fountain, D.M., Salisbury, M.H. & Furlong, K.P., 1987. Heat production and thermal conductivity of rocks from the Pikwitonei-Sachigo continental cross-section, central Manitoba: implications for the thermal structure of Archean crust. *Can. J. Earth Sci.,* **24,** 1583–1594.

Galetti, E., Curtis, A., Meles, G.A. & Baptie, B., 2015. Uncertainty loops in travel-time tomography from nonlinear wave physics, *Phys. Rev. Lett.,* **114**.

Galson, D.A., 1983. *Heat production in the Ivrea and Strona Ceneri zones*. PhD thesis, Univ. Cambridge, Cambridge, UK.

Hale, L.D. & Thomson, G.A., 1982. The seismic reflection character of the continental Moho discontinuity. *J. geophys. Res.,* **87,** 4625–4635.

Handy, M.R., 1987. The structure, age and kinematics of the Pogallo Fault Zone; Southern Alps, northwestern Italy. *Eclogae Geol. Helv.,* **80,** 593–632.

Hetényi, G., Vergne, J., Bollinger, L. & Cattin, R., 2011. Discontinuous low-velocity zones in southern Tibet question the viability of the channel flow model. *Geol. Soc., Lond., Spec. Publ.,* **353,** 99–108.

Horstmann, U., 1981. *Petrographische, tektonische und mikrothermometrische Untersuchungen an der Insubrischen Line im Val Sermenza (Provinz Vercelli, Norditalien),* Diploma thesis. University of Göttingen.

James, D.E., Niu, F. & Rokosky, J., 2003. Crustal structure of the Kaapvaal craton and its significance for early crustal evolution. *Lithos, 71,* 413–429.

Karakas, O. *et al.*, 2019. The pace of crustal-scale magma accretion and differentiation beneath silicic caldera volcanoes. *Geology, 47,* 719–723.

Kern, H. & Schenk, V., 1985. Elastic wave velocities in rocks from a lower crustal section in southern Calabria (Italy). *Phys. Earth planet. Inter., 40,* 147–160.

Khazanehdari, J., Rutter, E.H. & Brodie, K.H., 2000. High pressure/temperature seismic velocity structure of the mid- and lower-crustal rocks of the Ivrea-Verbano zone and Serie dei Laghi, NW Italy. *J. geophys. Res., 105,* 13843–13858.

Kissling, E., 1984. Three-dimensional gravity model of the northern Ivrea-Verbano Zone, Geomagnetic and Gravimetric Studies of the Ivrea Zone. in *Mater. Geol. Suisse. Geophys, Kümmerly & Frey,* pp. 55–61, eds. Wagner, J.J. & Müller, S., Geographischer Verlag, Bern.

Lanza, R., 1982. Models for interpretation of the magnetic anomaly of the Ivrea body. *Geol. Alpine, 58,* 85–94.

Liu, Y., Greenwood, A., Hetényi, G., Baron, L. & Holliger, K., 2021. High-resolution seismic reflection survey crossing the Insubric Line into the Ivrea-Verbano Zone: novel approaches for interpreting the seismic response of steeply dipping structures. *Tectonophysics, 816,* 229035. doi:10.1016/j.tecto.2021.229035.

Lu, Y., Stehly, L., Paul, A. & Group, A.W., 2018. High-resolution surface wave tomography of the European crust and uppermost mantle from ambient seismic noise. *Geophys. J. Int., 214*(2), 1136–1150.

Mazzucchelli, M., Rivalenti, G., Brunelli, D., Zanetti, A. & Boari, E., 2009. Formation of highly refractory dunite by focused percolation of pyroxenite-derived melt in the Balmuccia peridotite Massif (Italy). *J. Petrol., 50,* 1205–1233.

Mereu, R.S., Mueller, S. & Fountain, D.M., 1989. *Properties and Processes of Earth's Lower Crust,* Washington, DC: AGU Geophysical Monograph Series, Vol. **51,** 333pp.

Metropolis, N., Rosenbluth, M.N., Rosenbluth, A.W., Teller, A.H. & Teller, E., 1953. Equation of state calculations by fast computing machines. *J. Chem. Phys., 21,* 1087–1092.

Müntener, O. & Ulmer, P., 2006. Experimentally derived high-pressure cumulates from hydrous arc magmas and consequences for the seismic velocity structure of lower arc crust. *Geophys. Res. Lett., 33,* L21308. doi:10.1029/2006GL027629.

Nicolas, A., Hirn, A., Nicolich, R. & Polino, R., 1990. Lithospheric wedging in the western Alps inferred from the ECORS-CROP traverse. *Geology, 18,* 587–590.

Peressini, G., Quick, J.E., Sinigoi, S., Hofmann, A.W. & Fanning, M., 2007. Duration of a large mafic intrusion and heat transfer in the lower crust: a SHRIMP U–Pb Zircon study in the Ivrea–Verbano Zone (Western Alps, Italy). *J. Petrol., 48*(6), 1185–1218.

Piana, F. *et al.*, 2017a. Geology of piemonte region (NW Italy, Alps-Apennines junction zone). *J. Maps, 13,* 395–405.

Piana, F. *et al.*, 2017b. Geological map of Piemonte region at 1: 250,000 scale, explanatory notes. Memorie dell'Accademia delle Scienze di Torino, Serie V, *Cl. Sci. Fis., 41,* 2–148, ISSN:1120-1630.

Pistone, M., Müntener, O., Ziberna, L., Hetényi, G. & Zanetti, A., 2017. Report on the ICDP workshop DIVE (Drilling the Ivrea–Verbano zonE), *Sci. Dril., 23,* 47–56.

Pistone, M., Ziberna, L., Hetényi, G., Scarponi, M., Zanetti, A. & Müntener, O., 2020. Joint geophysical-petrological modelling on the Ivrea geophysical body beneath Valsesia, Italy: constraints on the continental lower crust. *Geochem. Geophys. Geosyst., 21,* e2020GC009397. doi:10.1029/2020GC009397.

Podvin, P. & Lecomte, I., 1991. Finite difference computation of traveltimes in very contrasted velocity models: a massively parallel approach and its associated tools, *Geophys. J. Int., 105,* 271–284.

Quick, J.E., Sinigoi, S. & Mayer, A., 1995. Emplacement of mantle peridotite in the lower continental crust, Ivrea-Verbano zone, northwest Italy. *Geology, 23,* 739–742.

Quick, J.E., Sinigoi, S., Negrini, L., Demarchi, G. & Mayer, A., 1992. Synmagmatic deformation in the underplated igneous complex of the Ivrea-Verbano zone. *Geology, 20,* 613–616.

Quick, J.E., Sinigoi, S., Peressini, G., Demarchi, G., Wooden, J.L. & Sbisa`, A., 2009. Magmatic plumbing of a large Permian caldera exposed to a depth of 25 km. *Geology, 37,* 603–606.

Quick, J.E., Sinigoi, S., Snoke, A.W., Kalakay, T.J., Mayer, A. & Peressini, G., 2002. Geologic map of the southern Ivrea-Verbano Zone, Northwestern Italy. US Geological Survey. doi:10.3133/i2776.

Rivalenti, G., Garuti, G. & Rossi, A., 1975. The origin of the Ivrea-Verbano basic formation (western Italian Alps): whole rock geochemistry: società Geologica Italiana, *Bollettino, 94,* 1149–1186.

Rivalenti, G., Garuti, G., Rossi, A., Siena, F. & Sinigoi, S., 1981. Existence of different peridotite types and of a layered igneous complex in the Ivrea Zone of the Western Alps: *J. Petrol., 22,* 127–153.

Rivalenti, G., Rossi, A., Siena, F. & Sinigoi, S., 1984. The layered series of the Ivrea-Verbano igneous complex, western Alps, Italy, *Tschermaks Mineral. Petrograph. Mitteilungen, 33,* 77–99.

Rudnick, R.L. & Fountain, D.M., 1995. Nature and composition of the continental crust: a lower crustal perspective. *Rev. Geophys., 33,* 267–309.

Rutter, E.H., Khazanehdari, J., Brodie, K.H., Blundell, D.J. & Waltham, D.A., 1999. Synthetic seismic reflection profile through the Ivrea zone–Serie dei Laghi continental crustal section, northwestern Italy. *Geology, 27,* 79–82.

Ryberg, T. & Haberland, Ch., 2018. Bayesian inversion of refraction seismic traveltime data, *Geophys. J. Int., 212,* 1645–1656.

Salisbury, M.H. & Fountain, D.M.eds., 1990. *Exposed Cross-Sections of the Continental Crust.* NATO ASI Series C, 317, ix + 662pp. Kluwer, Dordrecht Boston London.

Scarponi, M., Hetényi, G., Berthet, T., Baron, L., Manzotti, P., Petri, B., Pistone, M. & Müntener, O., 2020. New gravity data and 3D density model constraints on the Ivrea Geophysical Body (Western Alps). *Geophys. J. Int., 222,* 1977–1991.

Scarponi, M., Hetényi, G., Plomerová, J., Solarino, S., Baron, L. & Petri, B., 2021. Joint seismic and gravity data inversion to image intra-crustal structures: the Ivrea geophysical body along the Val Sesia Profile (Piedmont, Italy). *Front. Earth Sci., 9,* 671412. doi:10.3389/feart.2021.671412.

Schmid, S., Zingg, A. & Handy, M., 1987. The kinematics of movements along the Insubric Line and the emplacement of the Ivrea Zone. *Tectonophysics, 135,* 47–66.

Schmid, S.M., Kissling, E., Diehl, T., van Hinsbergen, D.J.J. & Molli, G., 2017. Ivrea mantle wedge, arc of the Western Alps, and kinematic evolution of the Alps–Apennines orogenic system. *Swiss J. Geosci., 110,* 581–612.

Schmid, S.M., Pfiffner, O.A., Froitzheim, N., Schönborn, G. & Kissling, E., 1996. Geophysical-geological transect and tectonic evolution of the Swiss-Italian Alps. *Tectonics, 15,* 1036–1064.

Schumacher, M.E., 1997. Geological interpretation of the seismic profiles through the Southern Alps (lines S1-S7 and C3 south), in *Deep Structure of the Swiss Alps Results from NRP 20,* pp. 101–114, eds. Pfiffner, A.O. *et al.*, Basel: Birkhäuser.

Shervais, J.W., 1979. Thermal emplacement model for the Alpine lherzolite massif at Balmuccia, Italy. *J. Petrol., 20,* 795–820.

Shervais, J.W. & Mukasa, S.B., 1991. The Balmuccia orogenic lherzolite massif, Italy. *J. Petrol.,* **Special_Volume**(2), 155–174. doi:10.1093/petrology/Special_Volume.2.155.

Shive, P.N. & Fountain, D.M., 1988. Magnetic mineralogy in an Archaean crustal section: implications for crustal magnetization. *J. geophys. Res., 93,* 12177–12186.

Sinigoi, S., Comin-Chiaramonti, P., Demarchi, G. & Siena, F., 1983. Differentiation of partial melts in the mantle: evidence from the Balmuccia peridotite. *Contrib. Mineral. Petrol., 82,* 351–359.

Sinigoi, S., Quick, J.E., Clemens-Knott, D., Mayer, A., Demarchi, G., Mazzucchelli, M., Negrini, L. & Rivalenti, G., 1994. Chemical evolution of a large mafic intrusion in the lower crust, Ivrea-Verbano Zone, northern Italy. *J. geophys. Res., 99*(B11), 21575–21590.

Sinigoi, S., Quick, J.E., Demarchi, G. & Klötzli, U., 2011. The role of crustal fertility in the generation of large silicic magmatic systems triggered by intrusion of mantle magma in the deep crust, *Contrib. Mineral. Petrol.,* **162,** 691–707.

Snoke, A.W., Kalakay, T.J., Quick, J.E. & Sinigoi, S., 1999. Development of a deep-crustal shear zone in response to syntectonic intrusion of mafic magma into the lower crust, Ivrea-Verbano Zone, Italy, *Earth planet. Sci. Lett.,* **166,** 31–45.

Souquière, F. & Fabbri, O., 2010. Pseudotachylites in the Balmuccia peridotite (Ivrea Zone) as markers of the exhumation of the southern Alpine continental crust. *Terra Nova,* **22,** 70–77.

Tryggvason, A. & Bergman, B., 2006. A traveltime reciprocity discrepancy in the Podvin & Lecomte time 3d finite difference algorithm. *Geophys. J. Int.,* **165,** 432–435.

Ueda, T., Obata, M., Ozawa, K. & Shimizu, I., 2020. The ductile-to-brittle transition recorded in the Balmuccia peridotite body, Italy: ambient temperature for the onset of seismic rupture in mantle rocks. *J. geophys. Res.,* **125**.

Vilhelm, J., Rudajev, V., Zivor, R., Lokajicek, T. & Pros, Z., 2008. Comparison of field and laboratory seismic velocity anisotropy measurements (scaling factor). *Acta Geodyn. Geomater.,* **5**(2), 161–169.

Voshage, H., Hofmann, A.W., Mazzuchelli, M., Rivalenti, G., Sinigoi, S., Raczek, I. & Demarchi, G., 1990. Isotopic evidence from the Ivrea Zone for a hybrid lower crust formed by magmatic underplating. *Nature,* **347,** 731–736.

Wasilewski, P.J. & Fountain, D.M., 1982. The Ivrea Zone as a model for the distribution of magnetization in the continental crust. *Geophys. Res. Lett.,* **9,** 333–336.

Wessel, P. & Smith, W., 1995. New version of the Generic Mapping Tools released, *EOS, Trans. Am. geophys. Un.,* **76,** 329. doi:10.1029/98EO00426.

Wessel, P. & Smith, W., 1998, New, improved version of the Generic Mapping Tool released, *EOS, Trans. Am. geophys. Un.,* **79,** 579. doi:10.1029/98EO00426.

Williams, M.C., Shive, P.N., Fountain, D.M. & Frost, B.R., 1985. Magnetic properties of exposed deep crustal rocks from the Superior Province of Manitoba. *Earth planet. Sci. Lett.,* **76,** 176–184.

Zingg, A., 1983. The Ivrea and Strona-Ceneri zones (Southern Alps, Ticino and N Italy): a review. *Schweiz. Mineral. Petrogr. Mitt.,* **63,** 361–392.

## SUPPORTING INFORMATION

Supplementary data are available at *GJI* online.

**seize-ra_supplement_final.docx**

Please note: Oxford University Press is not responsible for the content or functionality of any supporting materials supplied by the authors. Any queries (other than missing material) should be directed to the corresponding author for the paper.